Toxicology and Applied Pharmacology 260 (2012) 173–182

Contents lists available at SciVerse ScienceDirect

Toxicology and Applied Pharmacology

journal homepage: www.elsevier.com/locate/ytaap

Alteration of hepatic structure and oxidative stress induced by intravenous nanoceria

Michael T. Tseng [a,*], Xiaoqin Lu [a,1], Xiaoxian Duan [a,1], Sarita S. Hardas [b], Rukhsana Sultana [b], Peng Wu [c], Jason M. Unrine [d], Uschi Graham [e], D. Allan Butterfield [b,2], Eric A. Grulke [c], Robert A. Yokel [f,3]

[a] Dept of Anatomical Sciences & Neurobiology, University of Louisville, Louisville, Kentucky, USA
[b] Dept. of Chemistry, University of Kentucky, Lexington, Kentucky, USA
[c] Dept of Chemical and Materials Engineering, University of Kentucky, Lexington, Kentucky, USA
[d] Dept of Plant and Soil Sciences, University of Kentucky, Lexington, Kentucky, USA
[e] Center for Applied Energy Research, University of Kentucky, Lexington, Kentucky, USA
[f] Department of Pharmaceutical Sciences, University of Kentucky, Lexington, Kentucky, USA

ARTICLE INFO

Article history:
Received 15 December 2011
Revised 8 February 2012
Accepted 13 February 2012
Available online 20 February 2012

Keywords:
Biodistribution
Ceria
Electron microscopy
Granuloma
Kupffer cell
Liver

ABSTRACT

Beyond the traditional use of ceria as an abrasive, the scope of nanoceria applications now extends into fuel cell manufacturing, diesel fuel additives, and for therapeutic intervention as a putative antioxidant. However, the biological effects of nanoceria exposure have yet to be fully defined, which gave us the impetus to examine its systemic biodistribution and biological responses. An extensively characterized nanoceria (5 nm) dispersion was vascularly infused into rats, which were terminated 1 h, 20 h or 30 days later. Light and electron microscopic tissue characterization was conducted and hepatic oxidative stress parameters determined. We observed acute ceria nanoparticle sequestration by Kupffer cells with subsequent bioretention in parenchymal cells as well. The internalized ceria nanoparticles appeared as spherical agglomerates of varying dimension without specific organelle penetration. In hepatocytes, the agglomerated nanoceria frequently localized to the plasma membrane facing bile canaliculi. Hepatic stellate cells also sequestered nanoceria. Within the sinusoids, sustained nanoceria bioretention was associated with granuloma formations comprised of Kupffer cells and intermingling $CD3^+$ T cells. A statistically significant elevation of serum aspartate aminotransferase (AST) level was seen at 1 and 20 h, but subsided by 30 days after ceria administration. Further, elevated apoptosis was observed on day 30. These findings, together with increased hepatic protein carbonyl levels on day 30, indicate ceria-induced hepatic injury and oxidative stress, respectively. Such observations suggest a single vascular infusion of nanoceria can lead to persistent hepatic retention of particles with possible implications for occupational and therapeutic exposures.

Introduction

Ceria (CeO_2) has enjoyed a long history of industrial application as an abrasive. Wide-ranging uses have been developed for ceria, particularly when its redox characteristics are combined with preparation on a nanoscale. These include uses as a catalyst, in fuel cells and batteries and in potential nanomedicine applications (Alphonse and Ansart, 2009; Amin et al., 2011; Chen et al., 2006; HEI, 2001; Hirst et al., 2009; Masui et al., 2000; Park et al., 2008). While there is little indication of nanoceria-induced adverse environmental impact, interest in possible biological responses to this engineered nanomaterial (ENM) has been heightened.

Nanoceria has been shown to have poor oral bioavailability (He et al., 2010), although its uptake from both oral and pulmonary routes can result in some translocation into the vascular system through which it can be distributed to multiple organs and tissues (He et al., 2010). For therapeutic applications it may therefore require iv administration and so we have chosen to assess its distribution and biological responses after iv administration in this study. We previously observed ceria accumulation in the liver and spleen, and a relative

Abbreviations: AST, aspartate aminotransferase; ENM, engineered nanomaterial; EELS, electron energy loss spectroscopy; BET, Brunauer Emmett and Teller; STEM, scanning transmission electron microscopy; Ce, cerium ion; ICP-MS, inductively coupled plasma mass spectrometry; MDL, method detection limit; IHC, immunohistochemistry; PCNA, proliferating cell nuclear antigen; TUNEL, terminal transferase-mediated dUTP nick end-labeling; HR-TEM, high resolution transmission electron microscopy; EDS, energy dispersing X-ray spectroscopy; PC, protein carbonyls; GR, glutathione reductase; GPx, glutathione peroxidase; MnSOD, manganese superoxide dismutase; Hsp, heat shock protein; DLS, dynamic light scatter; H_2O_2, hydrogen peroxide.

* Corresponding author. Fax: +1 502 852 6228.
E-mail addresses: mttsen01@louisville.edu (M.T. Tseng), x0lu0003@louisville.edu (X. Lu), x0duan02@louisville.edu (X. Duan), sarita.hardas@uky.edu (S.S. Hardas), rsult2@uky.edu (R. Sultana), peng.wu@uky.edu (P. Wu), jason.unrine@uky.edu (J.M. Unrine), graham@caer.uky.edu (U. Graham), dabcns@uky.edu (D.A. Butterfield), eric.grulke@uky.edu (E.A. Grulke), ryokel@email.uky.edu (R.A. Yokel).
[1] Fax: +1 502 852 6228.
[2] Dept of Chemistry, Center of Membrane Sciences, University of Kentucky, Lexington, Kentucky 40506.
[3] Department of Pharmaceutical Sciences, College of Pharmacy, University of Kentucky, Lexington, Kentucky. Fax: +1 859 257 7564.

0041-008X/$ – see front matter © 2012 Elsevier Inc. All rights reserved.
doi:10.1016/j.taap.2012.02.008

lack of systemic tissue injury up to 20 h following a single, large dose of iv ceria infusion (Yokel et al., 2009). We also determined that ceria induced dose-dependent activation of Kupffer cells with subsequent nanoceria uptake into hepatocytes (Yokel et al., 2009). Kupffer cells residing along the hepatic sinusoidal lining are known to be the first macrophages to contact xenobiotic materials, such as an infusion of nanoceria, entering the liver from the hepatic portal vein (Dai et al., 2006; Sadauskas et al., 2009; Zhang et al., 2005). Additionally, the liver is known to be a major immunological organ affecting systemic responses in animals in response to xenobiotics, in part because of the abundance of mononuclear phagocytes (Si-Tayeb et al., 2010). In addition to phagocytosis and the eradication of foreign materials, the liver phagocytic system also produces an array of mediators, including arachidonic acid metabolites, cytokines, and reactive oxygen species, which protect the host against invasion by foreign organisms and xenobiotic chemicals (Algood et al., 2005; Ladel et al., 1995; Si-Tayeb et al., 2010).

For these reasons we chose to focus on the liver in our study of the systemic distribution and biological effects of an extensively characterized ceria nanoparticle. After a single iv infusion of 5 nm ceria, rats were examined for up to 30 days to determine acute, and possible longer term, hepatocellular responses to this metal oxide ENM. We observed persistent bioaccumulation of nanoceria with acute serum transaminase elevation, liver granuloma formation, elevated apoptosis, and increased levels of oxidative stress in the liver, which highlights potential nanoceria-induced adverse long term biological consequences.

Methods

Nanoscale ceria synthesis and characterization. Nanoscale ceria was synthesized as described previously (Masui et al., 2000). Synthesized ceria was centrifuged, washed with deionized ultra-filtered water, and air dried overnight to generate a powder sample for Brunauer, Emmett, and Teller (BET) surface area determination. The particle hydrodynamic diameter distribution of the synthesized ceria dispersion, as well as the ceria ENM morphology, crystallinity, surface area and zeta potential were determined as reported (Dan et al., 2012). Electron energy loss spectroscopy (EELS) was used to determine the cerium ion Ce(III)/Ce(IV) ratio from the M5/M4 ionization edges using a JEOL 2010-F Field Emission transmission electron microscopy (TEM). Scanning TEM (STEM) images were acquired using the high resolution probe at 2 Angstrom (Å) and EELS was performed using the 0.2 Å probe, alpha of 30 mrad, and a beta of 6 mrad. To avoid a possible electron beam interaction that could reduce cerium ions to the Ce(III) state, a less focused beam was used (Winterstein et al., 2008).

Animal care. For this study 58 male Sprague Dawley rats that weighed 324 ± 29 g (mean ± SD) at the time of experimentation, were obtained from Harlan Laboratories Inc. (Indianapolis, IN). Rats were housed individually prior to study and after vascular cannula removal, which occurred a few days after the iv infusion. Animals were housed at the University of Kentucky Division of Laboratory Animal Resources facility and given a 12 h light: dark cycle at a temperature of 70 ± 8 °F, and between 30 and 70% humidity. The rats had ad libitum access to 2018 Harlan diet and reverse osmosis water. Animal work was approved by the University of Kentucky Institutional Animal Care and Use Committee. The research was conducted in accordance with the Guiding Principles in the Use of Animals in Toxicology.

Nanoscale ceria infusion. A PE50 (0.023 in ID x 0.038 in OD) cannula was surgically inserted into the femoral veins of rats anesthetized with 75 mg/kg ketamine and 5 mg/kg xylazine ip, that was supplemented with 5 mg/kg ketamine ip as needed to maintain depth of anesthesia. Both femoral cannulae terminated in the vena cava, and one cannula was deliberately left 2 cm longer than the other. They were connected to an infusion pump via a flow-through swivel connector. This enabled administration of the ceria and observation of its effects in awake, mobile rats. The day after cannulation, unanesthetized rats were infused iv via the shorter cannula with a citrate-stabilized ceria dispersion. Rats were given approximately 85 mg/kg ceria as a 4% dispersion in water (estimated concentration of 40 mg/ml) delivered in a volume of 2 ml/kg over 1 h, or an equal volume of water as control with pH adjusted to 8 (Hardas et al., 2010). The dose of 85 mg/kg was selected as an initial dose to determine the long term distribution and effects of this nanoceria as we found in preliminary studies that this dose, delivered by this route of administration, was well tolerated by rats. To compensate for iv administration of a considerable volume of water, which may lead to grossly hypotonic ceria dispersion, we gave rats a concurrent iv infusion of an equal volume and rate of 1.8% sodium chloride solution in water through the longer cannula. Serum from rats euthanized at 1 h or 20 h after ceria infusion was clear, indicating that these infusions did not produce hemolysis. Ceria-infused rats were terminated at 1 h (n = 11), 20 h (n = 12) or 30 days (n = 10) after the end of the infusion. There were 7, 8, and 10 control rats per experimental group respectively.

Animal termination, tissue processing, and histopathology analysis. After termination of ketamine-anesthetized rats liver samples harvested from the tip of the median lobe were fixed in 10% neutral buffered formalin and processed for histopathology analysis. Sections (5 μm) were stained with hemotoxylin and eosin, and were examined for qualitative and quantitative changes. The size of the hepatic granulomata was digitally recorded, and the size of the involved liver tissue was measured with Neurolucida software (MBF Bioscience, Williston, VT) in a Nikon Eclipse E-800 microscope to tabulate granulomata density. The lesions were assessed on coded slides by an observer unaware of the experimental treatment.

Tissue ceria assay. Ceria concentrations were determined by measuring total cerium ion (Ce) analysis using microwave-assisted nitric acid/hydrogen peroxide digestion, and inductively coupled plasma mass spectrometry (ICP-MS) as described previously (Yokel et al., 2009). The mean method detection limit (MDL) of Ce in tissue was reported in that study as 0.089 mg/kg. Cerium concentrations that did not reach the MDL were reported here as 50% of the MDL for the purpose of data analysis.

Immunohistochemistry (IHC). Mononucleated cells in the liver parenchyma were determined by IHC using anti-CD3 rabbit monoclonal antibody (clone EP449E, Thermo Scientific, Fremont, CA). Briefly, 6 μm sections were deparaffinized, boiled in hot citrate buffer for antigen retrieval, and incubated with anti-CD3 antibody (at a concentration of 1:125) for 30 min at room temperature. Immunoreactive complexes were detected using the avidin–biotin affinity system (Santa Cruz Biotechnology, Santa Cruz, CA), and visualized with 3,3′-diaminobenzidine tetrahydrochloride (Zymed Laboratories, San Francisco, CA) as a substrate. The sections were counterstained with Mayer's hematoxylin and mounted with a cover slip. Controls included substitution of primary antibody with phosphate buffered saline and human thymus tissue as a positive tissue control.

Cell proliferation, degeneration, and apoptosis analyses. Possible nanoceria-induced cellular proliferation and degeneration were studied by proliferating cell nuclear antigen (PCNA) immunostaining and apoptosis by the terminal transferase-mediated dUTP nick end-labeling (TUNEL) method for determining DNA nicks, respectively. PCNA IHC detecting nuclear antigen synthesized in early G1 and S-phases of the cell cycle, and was used to assay for possible

nanoceria-induced cellular proliferation. Slides were boiled in hot citrate buffer for antigen retrieval, endogenous peroxidase activity was quenched with a 3% hydrogen peroxide solution, and non-specific binding was blocked with IgG-free bovine serum albumin (Jackson ImmunoResearch Laboratories, West Grove, PA). Sections were immunostained using a monoclonal anti-PCNA antibody (Santa Cruz Biotechnology) at dilution of 1:200 overnight at 4 °C. Signal was visualized using the avidin–biotin–peroxidase ABC kit (Vector Labs, Burlingame, CA) and 3, 3′-diaminobenzidine tetrahydrochloride (Vector Labs, Burlingame, CA) as the chromogen. Controls included substitution of primary antibody with phosphate buffered saline and human melanoma tissue as a positive tissue control. Deparaffinized slides were prepared for TUNEL assay according to the protocol supplied with the ApopTag Plus Peroxidase In Situ Apoptosis Detection Kit (S7101) (Millipore, Billerica, MA) and using a positive reaction control of DNase treatment, negative reaction control created by deleting the TdT enzyme, and positive tissue control with known active apoptotic components supplied by the manufacturer.

Serum biochemistry. To assess possible hepatotoxicity serum aspartate aminotransferase (AST) was measured using a commercial spectrophotometric diagnostic kit (Thermo Scientific). Briefly, blood samples were centrifuged at $1000 \times g$ for 10 min within 1 h after collection to generate serum, which was stored at −80 °C. Serum AST activity was determined by measuring ultraviolet kinetics, and read in a Biotek Synergy HT Plate reader (MTX Lab Systems, Inc., Vienna, VA), and the results expressed as U/L.

Electron microscopy. Immediately after excision, thin strips of liver samples were cut into 3 mm^3 pieces, dehydrated, and embedded in Araldite 502. Polymerized blocks of tissue were sectioned at 1 μm thickness and stained with toluidine blue for light microscopy screening. Selected blocks were sectioned, mounted on 200-mesh copper grids, and examined with a Phillips CM-10 electron microscope equipped with a LaB_6 cathode (Phillips Electronic Instruments Co. Eindhoven, The Netherlands) operated at 60 kV. For high resolution microscopy (HR-TEM), sections were collected on Formvar/carbon coated copper grids (200 mesh, Ted Pella Inc. Redding, CA) without staining for analysis in STEM mode, energy-dispersive X-ray spectroscopy (EDS), and EELS analysis in a JEOL 2010 TEM operated at 200 kV.

Pro-/anti-oxidative stress assessment. Liver samples obtained from rats at 30 days after ceria or saline treatment were evaluated for oxidative stress using methods previously described (Hardas et al., 2010). Briefly, each sample was individually thawed, homogenized using a 550 sonic dismembrator (Fisher Scientific) for 10–20 s on ice. Equal amounts of protein (250 ng) from control and treated samples were used in each antibody-based assay of the oxidative stress markers, protein carbonyls (PC), 3-nitrotyrosine, and protein bound 4-hydroxy-2-trans-nonenal. To determine the level of specific redox-related proteins, catalase, glutathione reductase (GR), glutathione peroxidase (GPx), manganese superoxide dismutase (MnSOD), heat shock protein (Hsp)32 (Hsp-32 or HO-1), and Hsp70 were determined by Western blot analysis, using 75 μg of sample per well. The activity of catalase, GR, GPx and MnSOD was determined in 10–20 μg sample aliquots.

Data analysis and statistics. For cell proliferation and degeneration analysis, the number of positive cells per high power field was tabulated. Statistical differences between two groups of parametric data were determined by one-way ANOVA and Tukey's multiple comparison post hoc tests for estimation of stochastic probability in inter-group comparisons (GraphPad Prism 5, La Jolla, CA). Comparison of oxidative stress results between groups was analyzed by one-tailed Student's *t*-test (SPSS, Chicago, Ill, USA). All results are presented as means ± SEM. Differences were considered to be statistically significant when the *p* values were less than 0.05.

Results

Nanoceria characterization

HR-TEM/HR-STEM analysis showed the ceria ENM was crystalline with polyhedral morphology (shape), with a number-average primary ceria particle size of approximately 5 nm (Fig. 1A). Dynamic light scattering (DLS) measurements showed that the average primary particle diameter was approximately 7.6 nm for both number- and volume-based (first peak) measurements. These data confirm a narrow particle size distribution with few agglomerates in the liquid phase (Figs. 1B and C). The ceria ENM surface area of the collected dried powder was 121 m^2/g, as measured by nitrogen adsorption (BET). Taking the density of ceria as 7600 kg/m^3 this surface area converts to an average primary particle diameter of 6.5 nm, which is in good agreement with the size measured by TEM and DLS methods. The mean of the lognormal model is shown as the average particle diameter (Fig. 1B). Volume-based ENM diameter averages are more meaningful regarding the dose received by the organism. Volume-based DLS results showed a bimodal distribution with one peak centered at 7.3 nm (98%) and another at 17.2 nm (2%) with most of nanoparticles well dispersed in water (Fig. 1C). The X-ray diffraction pattern analysis showed the ceria to be face-centered cubic with corresponding Miller indices of the most common faces of (111), (210) and (200). Zeta potential of the particles was −53 ± 7 mV at a pH of approximately 7.35.

Ten batches of aqueous ceria dispersion were analyzed in duplicate for Ce content by ICP-MS. This analysis showed the content to be 4.35 ± 0.20% in aqueous solution, indicating that the delivered dose was approximately 85 mg/kg. DLS analysis showed no change in average particle hydrodynamic diameter in 10% sucrose or in 0.9% saline over 20 h at room temperature, or at physiological temperature (37 °C) after 1 h.

HR-TEM-EELS spectra for ceria displayed two sharp features at 883 and 901 eV, corresponding to the cerium M5 and M4 ionization edges, respectively. EELS showed sharp intense M5 and M4 edges for both the as-synthesized 5 nm ceria (collected powder) (Fig. 1D), and ceria agglomerates in liver 30 days after infusion into rats (Figs. 2A and B). Differences in the peak height in EELS results are caused by the sample thickness in the mounted tissue material. The M5 and M4 ionization edge ratios showed very similar valence reduction of Ce ions for both the as-synthesized powder and the hepatic ceria agglomerates, with ratios of 1.09 and 1.20 respectively, suggesting significant oxygen vacancies exist in the ceria lattice.

Tissue ceria concentration

The cerium concentrations at 1 h, 20 h or 30 days after ceria infusion were 424 ± 297, 1007 ± 264, and 578 ± 336 mg/kg wet weight respectively in liver, and 270 ± 79, 12 ± 9, and 0.11 ± 0.16 mg/l respectively in blood. Using an estimated rat blood volume of 7% of its body weight, 27% and 22% of ceria was in blood and liver respectively at 1 h, 1.3% and 51% at 20 h, and 0.01% and 44% by 30 days after completion of ceria infusion. These data show clearance of ceria ENM from the blood into liver, and the persistence of ceria ENM in the liver. The remaining ceria was dispersed in other organs, including the spleen. Results from a similarly conducted study of a 30 nm ceria showed a distribution of 33%, 27%, 12%, 2.4%, 1.8%, 0.2%, and 0.2% of the ceria dose in the liver, bone marrow, spleen, skeletal system, lung, blood, and kidney respectively, with less than 0.2% in each of 8 other measured organs/body fluids 1 day after ceria infusion (Yokel et al., 2012). Of the 25 control rats, 5 had liver cerium concentration that exceeded the MDL, with levels ranging from 0.24 to 1.5 mg/kg.

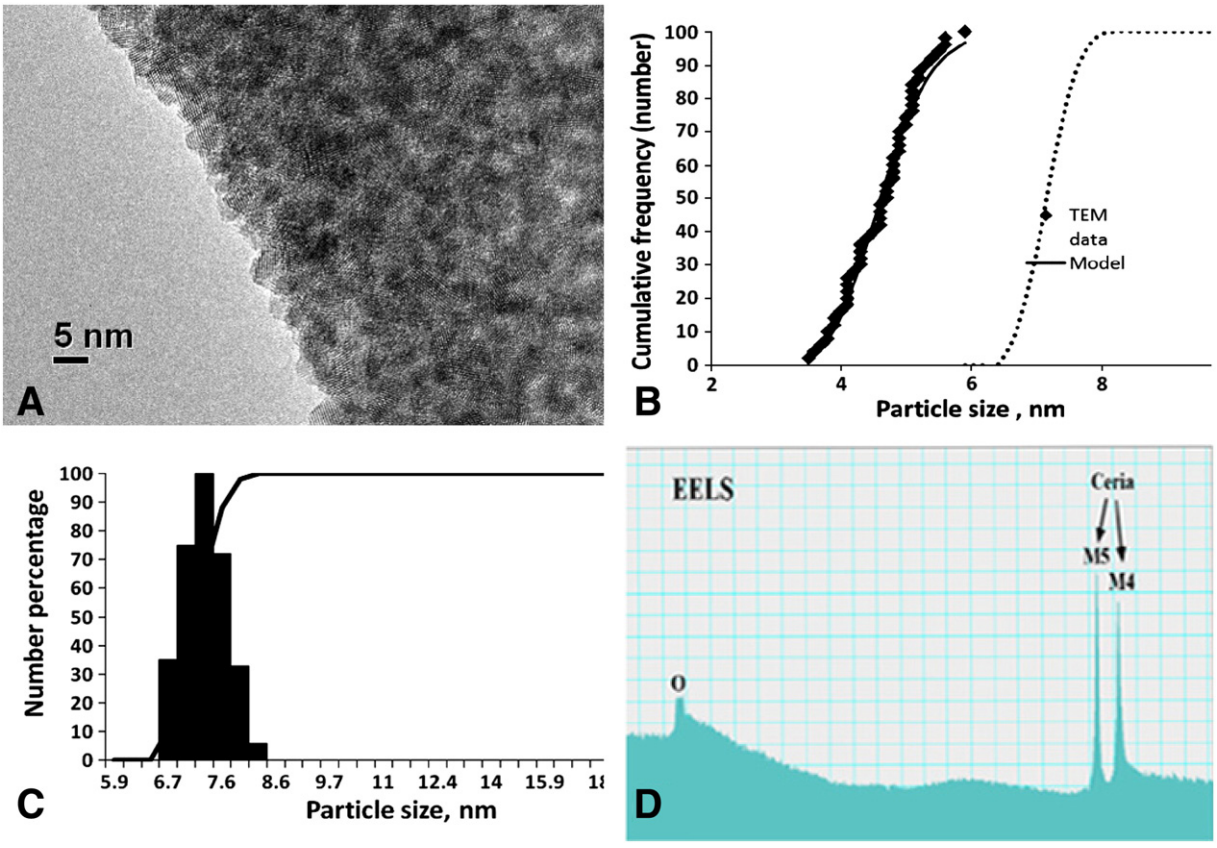

Fig. 1. Characterization of the as-synthesized 5 nm ceria. HR-TEM features of as synthesized ceria ENM (A). Number-based particle size distribution of ceria nanoparticles, as determined by TEM and DLS is shown (B). Diamond represents TEM data, and solid line is lognormal model. Dotted line represents the hydrodynamic diameter of ceria determined using DLS (B). The number-based hydrodynamic diameter of ceria nanoparticles determined by DLS is shown (C). EELS analysis showing ceria distinct M5 and M4 peaks before in vivo cellular uptake (D).

Hepatic response — light microscopy

In animals terminated 1 h or 20 h after ceria ENM infusion, the architecture of the liver (hepatocellular cords with distinct portal triads and central veins) appeared similar to those of the non-ceria infused controls (Fig. 3A). Neither Kupffer cells nor hepatocytes contained cytoplasmic particulates that were observable by light microscopy. However, in rats terminated on day 30 after ceria infusion, activated Kupffer cells had clearly visible accumulations of cytoplasmic particulates and were, intermingled with surrounding mononucleated cells to form granulomatous lesions (Figs. 3B, C). Similar sinusoidal granulomatous accumulations punctuated all ceria-infused rat livers examined at day 30. The size of the granulomata ranged from 132 to 4780 μm^2, with an average area of $1201 \pm 104\ \mu m^2$. The average frequency of the granuloma was 0.89 ± 0.59 granuloma/mm^2. By comparison, no granulomata were found in vehicle-infused rats. In addition to the granulomata, solitary Kupffer cells filled with nanoceria were identified without the encircling mononucleated cells, and were present in the hepatic

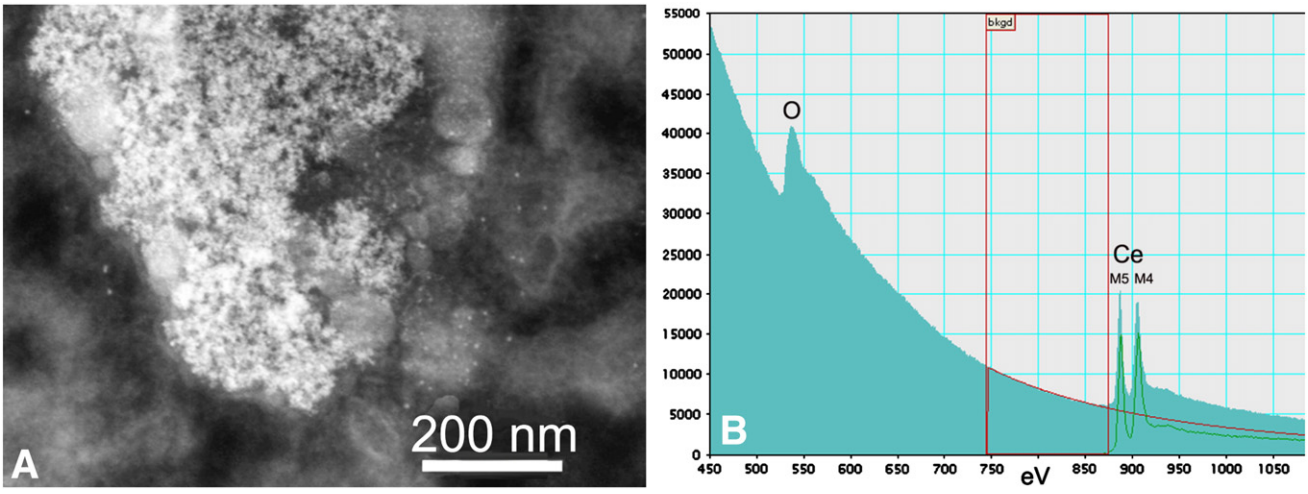

Fig. 2. Characterization of 5 nm ceria in liver. The agglomerated ceria ENM in a hepatocyte at 30 days after infusion (A), and an EELS spectrum with M5 and M4 peaks from similar agglomerate is illustrated (B).

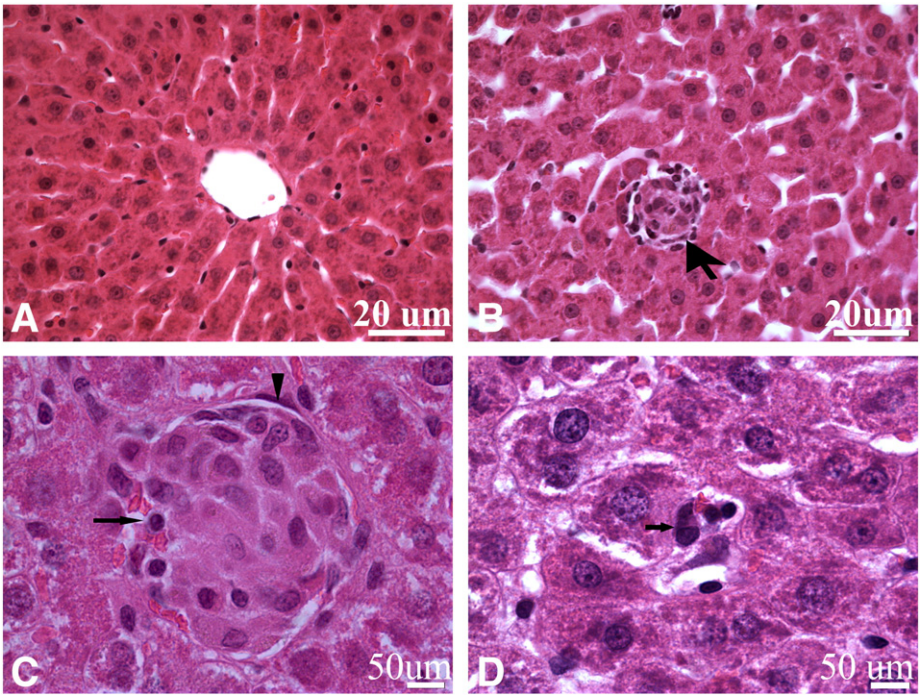

Fig. 3. Light microscopy features of the liver after ceria infusion. Normal histology was seen at 1 h and 20 h after control infusion. An image at 20 h is shown in A. Granulomatous formations (arrow) appeared only in 30-day samples in ceria-infused rats (B). At higher magnification cellular constituents of a granuloma, including large Kupffer cells, small lymphocytes with a round nucleus [arrow], and a surrounding endothelial cell [arrowhead] are shown C. Besides granulomatous formations, liver parenchyma also contained some dispersed Kupffer cells (arrow) (D).

sinusoids of 30-day rats (Fig. 3D). The nature of the encircling mononucleated cells in the hepatic granuloma was partially revealed by IHC with a pan T-cell antibody, anti-CD3, commonly used in immunophenotyping of lymphomas in paraffin sections (Wang et al., 2009). Our results show that $CD3^+$ cells were a component of the cellular ensheathment typical of ceria-induced granulomata (Figs. 4A, B).

Hepatic response — electron microscopy

At the ultrastructural level, uptake of nanoceria by Kupffer cells, stellate cells, and hepatocytes was detected at 1 h, 20 h or 30 days after nanoceria infusion. The infused ceria appeared as free flowing nanoceria agglomerates, which penetrated the subendothelial space

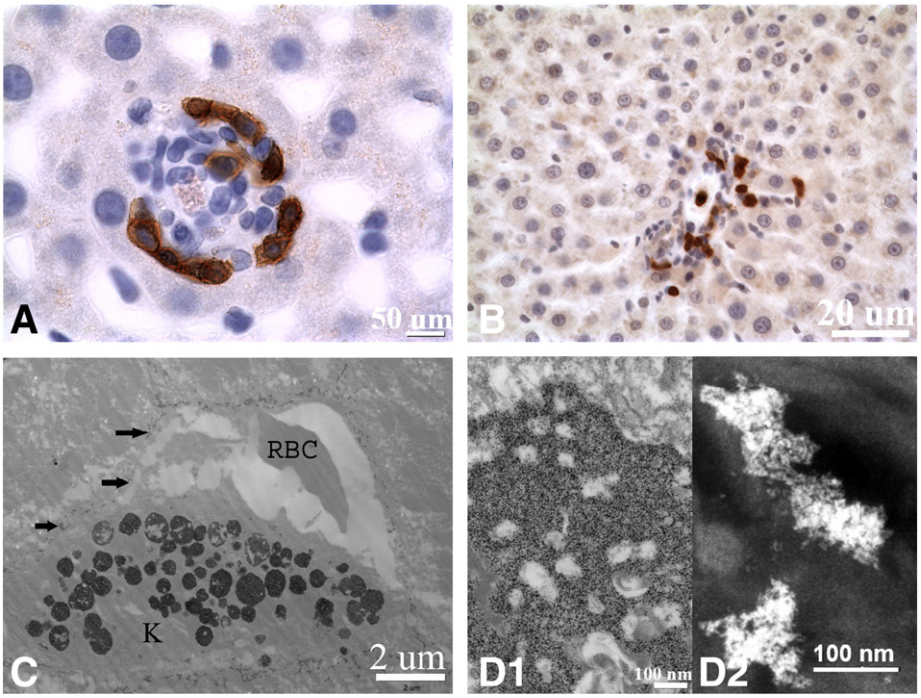

Fig. 4. Light microscopy, IHC and TEM features of ceria-exposed liver tissue. A population of brown staining, $CD3^+$, mononucleated cells in a granuloma (A). At a lower magnification, perivascular accumulation of $CD3^+$ cells (B). Biodistribution of ceria appeared as large, electron dense cytoplasmic agglomerates in a Kupffer cell (K), the presence of strands of ceria in the Space of Disse (arrows), but none in an erythrocyte (RBC) (C). Large agglomerates punctuated by a lightly stained cytoplasmic component are illustrated by TEM (D1). An HR-TEM/STEM image from a similar area demonstrates heterogeneity of the ceria agglomerate (D2).

of Disse, took on the appearance of a lacy network of electron dense particulates. One hour after infusion, the uptake of ceria in Kupffer cells ranged from small nanometer-sized clusters that included only a few ceria particles to agglomerates larger than 1 μm (Fig. 4C) appeared. The large agglomerates were made up of highly electron dense spherical to oblong-shaped ceria accumulations consisting of closely packed ceria particles. The large ceria agglomerates were typically separated by an amorphous, less electron dense, matrix material (Fig. 4D1). The ceria particles appeared as bright agglomerates against the dark background in HR-TEM/STEM imaging mode (Fig. 4D2). The circulating nanoceria particulates often abutted erythrocytes, but they appeared not to be retained by circulating erythrocytes. Careful examination of the surface of the hepatocyte revealed endocytosis of nanoceria through flask-shaped caveolar pits (Fig. 5A). Once internalized, the agglomerated particles were not often membrane enclosed. In the subendothelial space, some hepatic stellate cells also exhibited nanoceria uptake. They can be differentiated from other cells by their spindle profile and the trend of containing one or more large lipid droplets (Warren et al., 2011) (Fig. 5B). Beyond the vascular compartment, nanoceria penetrated the hepatocytes, where internalized ceria rarely appeared as individual primary 5 nm particles, and cytoplasmic agglomerates appeared more uniform in dimension but seldom exceeded 150 nm in diameter.

At 20 h after ceria infusion, hepatocyte retention of ceria continued. The cytoplasmic distribution of the accumulated ceria agglomerates appeared random. They were not retained in mitochondria or within the cell nucleus (Fig. 5C). Although many agglomerates appeared near the bile canaliculi, active translocation of ceria particles into the biliary system was not observed. When viewed in HR-TEM/STEM mode the ceria ENM agglomerates appeared brightly lit against the background cytoplasm (Fig. 5D). A few ceria particles were occasionally found within a lysosome (Fig. 5D, inset).

In day 30 liver samples, large ceria-agglomerate-engulfing Kupffer cells together with encircling smaller mononucleated cells formed sinusoidal granulomata. Within a single granuloma, one or more Kupffer cells were found (Fig. 6A). Electron dense ceria agglomerates were most abundant in Kupffer cells, and at times occupied a large portion of the phagocyte's cytoplasm (Fig. 6B). The size of these agglomerates exceeded 2 μm in diameter at times. Some ceria agglomerates were membrane-enclosed with heterogeneous electron dense particles. Many Kupffer cell nuclei appeared pyknotic, with large patches of heterochromatin. Although some non-Kupffer cells also enclosed ceria nanoparticles, they were devoid of large agglomerates (Fig. 6C). Aside from the presence of large sinusoidal granuloma, solitary Kupffer cells with electron dense ceria agglomerates also persisted. In the hepatocellular plate, the majority of hepatocytes adjacent to these solitary Kupffer cells were devoid of ceria particulates (Fig. 6D).

Liver enzyme activity and hepatic cell turnover

Elevated serum AST levels indicate acute hepatotoxicity. Serum AST levels at 1 h and 20 h after ceria infusion were statistically significantly higher than controls. However, the AST elevation subsided by day 30 in ceria infused rats. One way ANOVA with Tukey's multiple comparison post-hoc analysis showed statistical difference ($p<0.05$) among the following study groups: 1 h ceria vs control; 20 h ceria vs control; 1 h ceria vs 30-day ceria; and 20 h ceria vs 30-day ceria (Fig. 7A). Nanoceria also affected hepatocellular programmed cell death in liver as revealed by TUNEL assay. Apoptotic cells were seen in all samples after the ceria infusion. While the majority of apoptotic cells were hepatocytes, degenerating mononucleated cells were also found in the granulomata. The persistence of ceria in the liver at 30 days after ceria infusion was associated with significant elevation of apoptotic cell counts (Fig. 7B). In spite of the nanoceria-induced increased programmed cell death, PCNA cell proliferation analysis showed no clear trend. Immunohistochemistry data indicated the percentage of proliferating cells was slightly

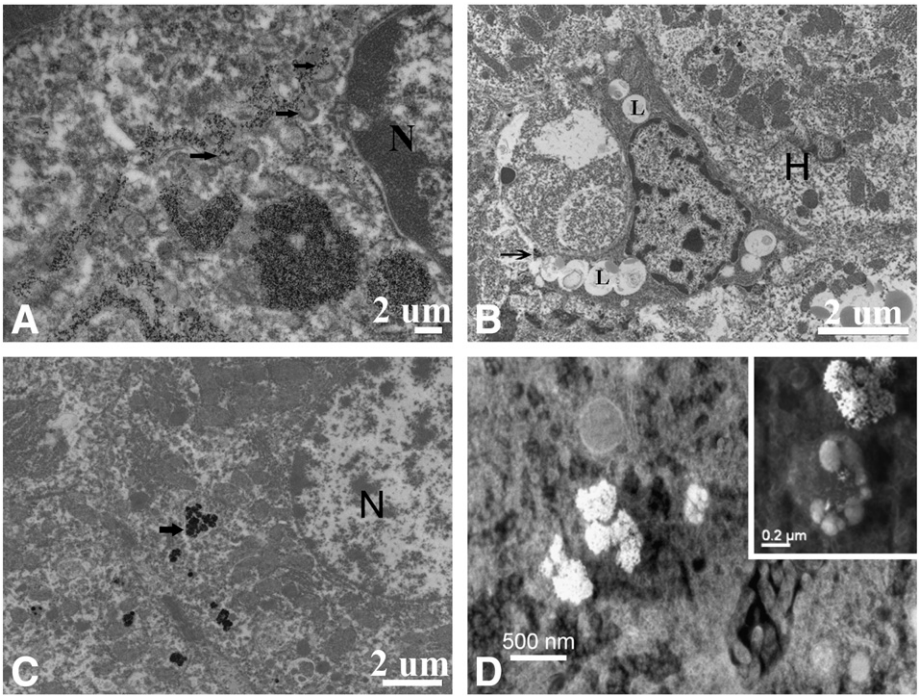

Fig. 5. Ultrastructure features of the cellular processing of nanoceria. Ceria nanoparticle uptake through endocytic vesicles is indicated by arrows (A). Adjacent to a hepatocyte (H) a hepatic stellate cell with fat droplets (L) and ceria agglomerate (arrow) is shown (B). Nanoceria agglomerates accumulated in hepatocytes (arrow) are illustrated (C). N = nucleus. A similar view of a ceria-containing hepatocyte by HR-TEM/STEM is shown (D). The inset demonstrates inclusion of a few ceria particles in a lysosome.

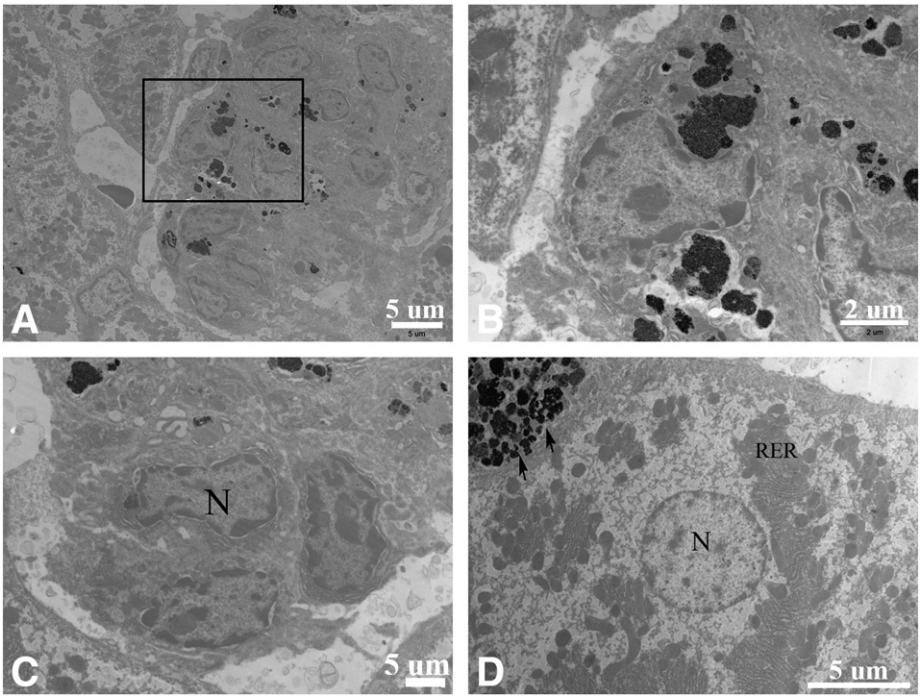

Fig. 6. Ultrastructural features of ceria-induced hepatic granuloma. Cellular heterogeneity of a granuloma is illustrated in panel A. The boxed area enlarged shows cells with patches of nuclear heterochromatin and a complement of large ceria agglomerates (B). Several mononucleated cells lacking ceria uptake are shown in C. Adjacent to the granuloma, a hepatocyte without ceria retention is shown (D). Note the large round nucleus (N), the highly developed rough endoplasmic reticulum (RER) and a contiguous Kupffer cell laden with ceria ENM (arrows).

elevated at 1 h and 20 h after ceria infusion, before settling to a level comparable to those of the controls on day 30 (Fig. 7C).

Oxidative stress assessment

Oxidative stress parameters in liver samples obtained following ceria treatment in rats were evaluated after 30 days only, as marked hepatocellular changes with persisting ceria accumulation were seen at this time point. Among the markers assessed (PC, 3-nitrotyrosine, and protein bound 4-hydroxy-2-trans-nonenal), a significant increase was observed only in PC levels (Fig. 8A). There was also a slight, but significant, decrease in liver catalase and GPx activities at 30 days after ceria infusion (Figs. 8B and C). Among the six antioxidant-related proteins analyzed (catalase, GR, GPx, MnSOD, Hsp32 and Hsp70), only Hsp32 levels were elevated significantly in the liver following ceria treatment compared with controls (Fig. 8D).

Discussion

This time-course study of ceria ENM bioaccumulation in the liver was conducted using an in-house synthesized and extensively-characterized nanoceria. In contrast to our earlier report using a 30 nm nanoceria (Yokel et al., 2009), the cellular uptake of the 5 nm ceria could not be discerned by light microscopy. This finding is consistent with previous reports concerning the influence of the size, shape, and surface properties on bioreactivity of nanomaterials (Alexis et al., 2008; Limbach et al., 2005; Wick et al., 2007). While the infused 5 nm ceria appeared to be rapidly taken up by the sinusoidal Kupffer cells, a portion of it remained in circulation for 20 h. During this time nanoceria appeared as large patches of electron dense material, or as a lacy network of particulates that penetrated the fenestrated endothelium of the sinusoids. Small caveolae-like vesicles observed on ceria-containing cell surfaces suggested a caveolae-dependent endocytosis cellular uptake (Peng et al., 2011; Sadauskas et al., 2007).

The observed nanoceria penetration was temporally correlated with an initial elevation of AST. Elevation of another liver transaminase, alanine aminotransferase, has also been reported after intratracheal cerium oxide instillation in rats (Nalabotu et al., 2011). In addition to Kupffer cell and endothelial cell affinity for nanoceria, the hepatic stellate cells also showed nanoceria accumulation. Interestingly, even as they accumulated nanoceria, they still retained a spindle-shaped cell profile, although their role in the metabolic processing of the infused nanoceria remains to be defined. It is plausible that the continued presence of nanoceria in hepatic stellate cells could trigger liver fibrosis over time (Zhan et al., 2006).

Analysis of hepatocellular ceria uptake showed that nanoceria displayed no specific organelle affinity, and remained as spherical, or irregularly-shaped, cytoplasmic agglomerates. The majority of the internalized nanoceria in hepatocytes showed little lysosomal interaction, although some lysosomes contained a few nanoceria particles. The relative lack of hepatic injury is consistent with the findings of lesser toxicity associated with cytoplasmic distribution of internalized nanoparticles versus those abundantly contained in the lysosomal compartment (Asati et al., 2010).

Frequent alignment of ceria agglomerates near the bile canaliculi suggested possible disposal or clearance attempts by hepatocytes to send ceria particles into the biliary system via bile canaliculi. However, consistent with our ICP-MS ceria assay data using 30 nm ceria (Yokel et al., 2012), ceria was not significantly excreted through this effluent pathway.

In spite of the trend of increased hepatocellular apoptosis, cell proliferation did not ensue, as indicated by the PCNA data. Moreover, necrotic foci within the liver were not observed. This is consistent with a lack of elevated AST on day 30. Nevertheless, continued presence of nanoceria particles causing increased hepatotoxicity could not be ruled out should the study duration is extended beyond 30 days. The lack of frank necrosis, is however, tempered by the formation of sinusoidal granulomata.

The presence of hepatic granulomata containing enduring nanoceria in Kupffer cells is an important observation. The formation of

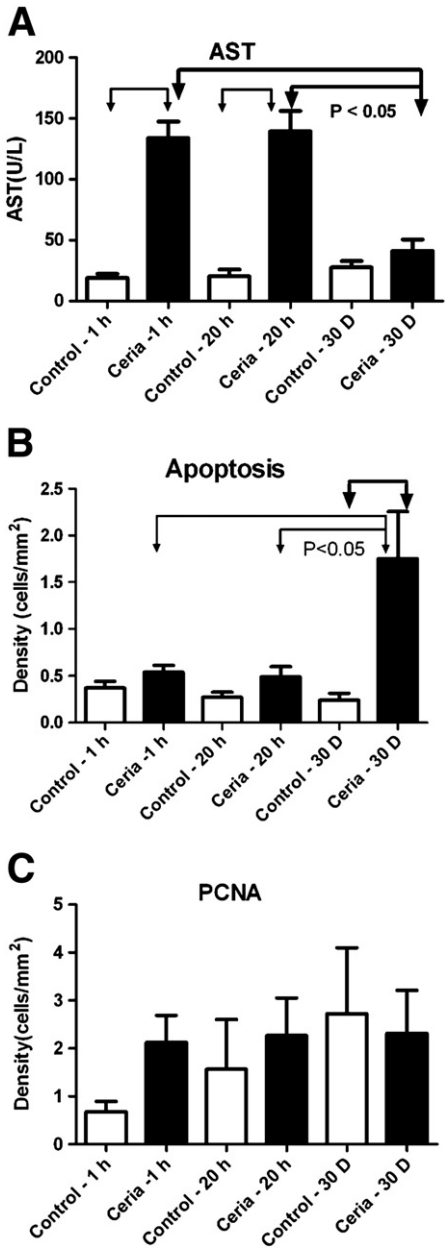

Fig. 7. Ceria induced changes in serum enzyme level and cell kinetics. Levels of AST at 1 h, 20 h and 30 days after ceria infusion (A) (*$p<0.05$). Density of apoptotic cells at 1 h, 20 h and 30 days after ceria infusion (B) (*$p<0.05$). PCNA labeled cell density in control and ceria-infused groups (C).

inflammatory granulomata is an innate immune response designed to isolate xenobiotics. As foci for recruiting and concentrating foreign materials, these phagocytic cell-rich aggregates limit inflammatory or host tissue damage (Kaufmann et al., 1995; Ohtomo et al., 2000). Inhalation of nanosized metal oxide containing single wall carbon nanotubes (SWCNTs) has been known to induce granulomatous formations in the lung, with parallel cytokine and chemokine modulations (Lam et al., 2004; Park et al., 2011). Thus, the nanoceria-induced granuloma formation in hepatic sinusoids could carry similar significant health implications. To document their presence, we used a combination of light microscopy, TEM and HR-TEM/STEM/EDS to provide a clear view of their cellular constituents, to confirm the elemental nature of the agglomerates, and through CD3 immunohistochemistry, demonstrate a link to the host immunological system. In our study, neutrophils were not histologically prominent. Mononuclear phagocytes (primarily resident macrophages) predominated to form the multinucleated core of these focal collections of aggregated cells. Critical to the generation and maintenance of a protective mycobacterial granuloma is the crosstalk between antigen-specific $CD4^+$ T cells and infected macrophages that produce an effector response in the macrophages to prevent replication and/or mediate killing of intracellular bacteria (Hansch et al., 1996; Ladel et al., 1995). Similar to our observation of the clearing of infused nanoceria in the vasculature, Bacille Calmette-Guérin was rapidly cleared from the blood through direct capture and phagocytosis by Kupffer cells (Kaklamanos et al., 2011; Kaufmann et al., 1995). And like our findings with nanoceria, these infected phagocytes persisted in the liver for several weeks after infection. The granulomatous response apparently evolved in host antimicrobial defense as a specialized tissue mechanism quite separate from abscess formation, and is capable of exerting largely beneficial but also potentially destructive actions. In our study the persistent bioaccumulation of nanoceria, like those provided by a spectrum of microbes (Beattie et al., 2010; Murray and Nathan, 1999; Saunders and Cooper, 2000), could serve as an intracellular pathogen/irritant associated with granulomatous inflammation. The presence of CD3 + T cells, and other additional critical cells, such as antigen-presenting dendritic cells or cytokine-secreting T cells, may be essential for granuloma formation (Schreiber et al., 2010). Lastly, it should be pointed out that the uptake of nanoceria by hepatic stellate cells, a cell subpopulation known to be associated with chronic liver diseases (Kim et al., 2010), may lead to fibrosis and cirrhosis over longer period of ceria exposure/bioretention.

Our analysis of oxidative stress parameters revealed reduced activity of catalase and GPx enzyme activities in liver tissue 30 days after ceria ENM treatment, in contrast to the elevated levels of PC and Hsp32. Other investigators have reported decreased GPx activity in mammalian liver upon treatment with ROS or RNS donor agents (Asahi et al., 1995; de Haan et al., 1998; Taniguchi et al., 1999), and that decreasing the activity of GPx made cells more susceptible to hydrogen peroxide-induced oxidative stress (Toussaint et al., 1993). In a rat model, inhibition of catalase by aminotriazole resulted in acute nephrotoxicity (Shaikh et al., 1999), whereas induction of catalase by an adenovirus gene delivery method showed protection against carbon tetrachloride- and ischemia-induced hepatic cell injury (Ushitora et al., 2010). Nanoceria has been reported to act like a SOD mimetic, that is, it is able to dismutate superoxide radicals into hydrogen peroxide (H_2O_2) and oxygen (Korsvik et al., 2007). Cerium ions are redox active and reported to undergo a Fenton-type reaction to produce hydroxyl radicals in the presence of H_2O_2 (Heckert et al., 2008). Catalase and GPx can reduce H_2O_2 into water and oxygen, therefore reduction in their activity may increase cellular H_2O_2 levels. According to our EELS analysis, the 5 nm ceria ENM had enriched Ce III, which may induce hydroxyl radical generation from such increased H_2O_2 levels. The observed increase in PC levels in the liver at 30 days after ceria treatment is consistent with this hypothesis. A caveat of this latter statement is that the relative increases in oxidative stress markers are small. Hence, caution should be exercised to not over-interpret these results.

Induction in oxidative stress markers and imbalance in oxidative stress may serve as an initiator for cytoprotective signal transduction, such as induction of stress-induced heat shock proteins (Goldberg, 2003; Poon et al., 2004). Investigators reported that cytotoxic effects of cobalt chloride treatment resulted in decreased catalase and GPx activities, which were compensated for by Hsp32 induction in rat liver (Llesuy and Tomaro, 1994). Hsp32 is a component of a cytoprotective pathway against oxidative stress and inflammation as shown in various animal and cell models (Poon et al., 2004; Siciliano et al., 2011; Yun et al., 2010). In the current study employing 5 nm ceria, Hsp32 levels in the liver were significantly upregulated in ceria ENM-treated rats. This induction of Hsp32 could be a response to oxidative stress, in particular a response to the decreased catalase and

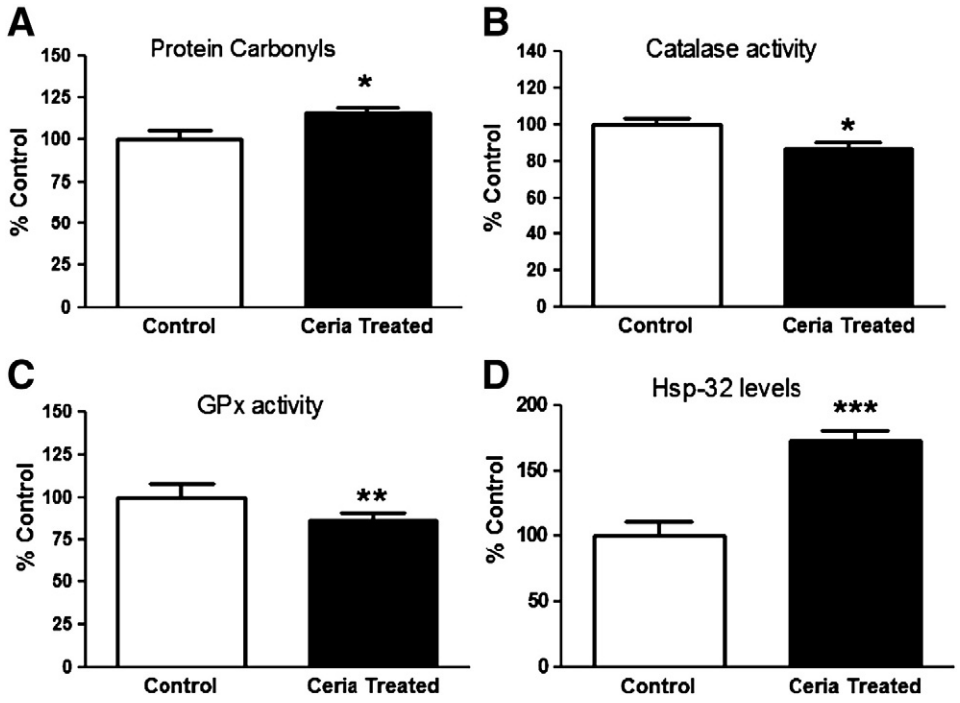

Fig. 8. Ceria-induced oxidative stress marker changes. Levels of PC (A), catalase activity (B), (*$p<0.05$) GPx activity (C) (**$p<0.005$) and Hsp32 (D) (***$p<0.001$) are shown. The intensity of the Hsp32 band was normalized to the control (actin) band.

GPx activities, as well as increased PC levels. Tissue injury, including apoptosis, has been linked to reactive oxygen species formation in cadmium-induced hepatic dysfunction and in fetal cardiac myocytes (Pal et al., 2011; Sinha-Hikim et al., 2011).

The morphological delineation of nanoceria uptake and translocation coupled with the study of oxidative indices from this time-course study clearly indicate that once ceria ENM gains systemic entrance to an organ rich in reticuloendothelial cells, it can persist for an extended period causing hepatic toxicity, cell turnover, lingering oxidative stress, and some immunologic responses. The prevalent granuloma formation at 30 days after a single nanoceria exposure and the increased apoptosis suggest the inability to eliminate nanoceria, which is supported by our unpublished metabolic data, and that the persistent retention of the internalized metal oxides among the surviving cells is undesirable. The reported hepatotoxicity in rats that received one intratracheal instillation of nanoceria and the decline in cognitive measurements in rats exposed to diesel exhaust nanoparticles, lend support to the issue of adverse biological consequences of xenobiotic retention (Nalabotu et al., 2011; Yokota et al., 2011). Hepatic damage induced by nanoceria in this study was indicated by the elevation of AST at 1 h and 20 h after ceria infusion. Decreasing levels of hepatic transaminases, and a well-maintained hepatic cytology offer hope that the observed hepatotoxicity may be limited. The lack of organelle penetration by ceria ENM may contribute to the relative lack of long-term cytotoxicity and could allow this ENM to function as an intracellular free radical scavenger (Chen et al., 2006; Pierscionek et al., 2010). While indication of similar health effects in the human has not been reported, our study, together with reports on nanoparticle-induced granuloma formation in the lung (Liao et al., 2008; Park et al., 2009), suggests a need for additional investigation of the potential health effects of nanoceria. In light of the increasing industrial, and proposed medical, applications of nanoceria, the observed hepatotoxicity raises safety concerns and invites future discovery of novel solutions for the enhanced metabolic processing of this and other ENMs by hepatocytes, Kupffer cells and stellate cells.

Conflict of interest

None of the authors has a financial conflict of interest related to this research.

Acknowledgments

This work was supported by United States Environmental Protection Agency Science to Achieve Results [grant number RD-833772]. Although the research described in this article has been funded wholly or in part by the United States Environmental Protection Agency through STAR Grant RD-833772, it has not been subjected to the Agency's required peer and policy review and therefore does not necessarily reflect the views of the Agency and no official endorsement should be inferred.

References

Alexis, F., Pridgen, E., Molnar, L.K., Farokhzad, O.C., 2008. Factors affecting the clearance and biodistribution of polymeric nanoparticles. Mol. Pharm. 5, 505–515.
Algood, H.M., Lin, P.L., Flynn, J.L., 2005. Tumor necrosis factor and chemokine interactions in the formation and maintenance of granulomas in tuberculosis. Clin. Infect. Dis. 41 (Suppl 3), S189–S193.
Alphonse, P., Ansart, F., 2009. Catalytic coating on steel for low temperature propane prereforming to solid oxide fuel cell (SOFC) application. J. Colloid Interface Sci. 336, 658–666.
Amin, K.A., Hassan, M.S., Awad el, S.T., Hashem, K.S., 2011. The protective effects of cerium oxide nanoparticles against hepatic oxidative damage induced by monocrotaline. Int. J. Nanomed. 6, 143–149.
Asahi, M., Fujii, J., Suzuki, K., Seo, H.G., Kuzuya, T., Hori, M., Tada, M., Fujii, S., Taniguchi, N., 1995. Inactivation of glutathione-peroxidase by nitric oxide implication for cytotoxicity. J. Biol. Chem. 270, 21035–21039.
Asati, A., Santra, S., Kaittanis, C., Perez, J.M., 2010. Surface-charge-dependent cell localization and cytotoxicity of cerium oxide nanoparticles. ACS Nano 4, 5321–5331.
Beattie, L., Peltan, A., Maroof, A., Kirby, A., Brown, N., Coles, M., Smith, D.F., Kaye, P.M., 2010. Dynamic imaging of experimental *Leishmania donovani*-induced hepatic granulomas detects Kupffer cell-restricted antigen presentation to antigen-specific CD8 T cells. PLoS Pathog. 6, e1000805.
Chen, J., Patil, S., Seal, S., McGinnis, J.F., 2006. Rare earth nanoparticles prevent retinal degeneration induced by intracellular peroxides. Nat. Nanotechnol. 1, 142–150.

Dai, H., Jiang, X., Tan, G.C., Chen, Y., Torbenson, M., Leong, K.W., Mao, H.Q., 2006. Chitosan-DNA nanoparticles delivered by intrabiliary infusion enhance liver-targeted gene delivery. Int. J. Nanomedicine 1, 507–522.
Dan, M., Wu, P., Grulke, E.A., Graham, U.M., Unrine, J.M., Yokel, R.A., 2012. Ceria engineered nanomaterial distribution in and clearance from blood: size matters. Nanomedicine 7, 95–110.
de Haan, J.B., Bladier, C., Griffiths, P., Kelner, M., O'Shea, R.D., Cheung, N.S., Bronson, R.T., Silvestro, M.J., Wild, S., Zheng, S.S., Beart, P.M., Hertzog, P.J., Kola, I., 1998. Mice with a homozygous null mutation for the most abundant glutathione peroxidase, Gpx1, show increased susceptibility to the oxidative stress-inducing agents paraquat and hydrogen peroxide. J. Biol. Chem. 273, 22528–22536.
Goldberg, A.L., 2003. Protein degradation and protection against misfolded or damaged proteins. Nature 426, 895–899.
Hansch, H.C., Smith, D.A., Mielke, M.E., Hahn, H., Bancroft, G.J., Ehlers, S., 1996. Mechanisms of granuloma formation in murine Mycobacterium avium infection: the contribution of CD4 + T cells. Int. Immunol. 8, 1299–1310.
Hardas, S.S., Butterfield, D.A., Sultana, R., Tseng, M.T., Dan, M., Florence, R.L., Unrine, J.M., Graham, U.M., Wu, P., Grulke, E.A., Yokel, R.A., 2010. Brain distribution and toxicological evaluation of a systemically delivered engineered nanoscale ceria. Toxicol. Sci. 116, 562–576.
He, X., Zhang, H., Ma, Y., Bai, W., Zhang, Z., Lu, K., Ding, Y., Zhao, Y., Chai, Z., 2010. Lung deposition and extrapulmonary translocation of nano-ceria after intratracheal instillation. Nanotechnology 21, 285103.
Heckert, E.G., Seal, S., Self, W.T., 2008. Fenton-like reaction catalyzed by the rare earth inner transition metal cerium. Environ. Sci. Technol. 42, 5014–5019.
HEI, Health Effects Institute, 2001. Evaluation of human health risk from cerium added to diesel fuel. : Communication, 9. Boston, MA USA.
Hirst, S.M., Karakoti, A.S., Tyler, R.D., Sriranganathan, N., Seal, S., Reilly, C.M., 2009. Anti-inflammatory properties of cerium oxide nanoparticles. Small 5, 2848–2856.
Kaklamanos, M., Hardavella, G., Trigidou, R., Dionellis, G., Paissios, N., Koulouris, N., Goritsas, C., 2011. Multi-organ failure with atypical liver granulomas following intravesical Bacillus Calmette-Guerin instillation. World J. Hepatol. 3, 79–82.
Kaufmann, S.H., Ladel, C.H., Flesch, I.E., 1995. T cells and cytokines in intracellular bacterial infections: experiences with Mycobacterium bovis BCG. CIBA Found. Symp. 195, 123–132 discussion 132–126.
Kim, Y.K., Lee, Y.H., Kwak, H.S., Kim, C.S., Han, Y.M., 2010. Detection of liver metastases: gadoxetic acid-enhanced three-dimensional MR imaging versus ferucarbotran-enhanced MR imaging. Eur. J. Radiol. 73, 131–136.
Korsvik, C., Patil, S., Seal, S., Self, W.T., 2007. Superoxide dismutase mimetic properties exhibited by vacancy engineered ceria nanoparticles. Chem. Commun. 1056–1058.
Ladel, C.H., Daugelat, S., Kaufmann, S.H., 1995. Immune response to Mycobacterium bovis bacille Calmette Guerin infection in major histocompatibility complex class I- and II-deficient knock-out mice: contribution of CD4 and CD8 T cells to acquired resistance. Eur. J. Immunol. 25, 377–384.
Lam, C.W., James, J.T., McCluskey, R., Hunter, R.L., 2004. Pulmonary toxicity of single-wall carbon nanotubes in mice 7 and 90 days after intratracheal instillation. Toxicol. Sci. 77, 126–134.
Liao, C.M., Chiang, Y.H., Chio, C.P., 2008. Model-based assessment for human inhalation exposure risk to airborne nano/fine titanium dioxide particles. Sci. Total. Environ. 407, 165–177.
Limbach, L.K., Li, Y., Grass, R.N., Brunner, T.J., Hintermann, M.A., Muller, M., Gunther, D., Stark, W.J., 2005. Oxide nanoparticle uptake in human lung fibroblasts: effects of particle size, agglomeration, and diffusion at low concentrations. Environ. Sci. Technol. 39, 9370–9376.
Llesuy, S.F., Tomaro, M.L., 1994. Heme oxygenase and oxidative stress — evidence of involvement of bilirubin as physiological protector against oxidative damage. Biochi. Biophys. Acta, Mol. Cell. Res. 1223, 9–14.
Masui, T., Ozaki, T., Machida, K., Adachi, G., 2000. Preparation of ceria-zirconia subcatalysts for automotive exhaust cleaning. J. Alloys Compd. 33, 49–55.
Murray, H.W., Nathan, C.F., 1999. Macrophage microbicidal mechanisms in vivo: reactive nitrogen versus oxygen intermediates in the killing of intracellular visceral *Leishmania donovani*. J. Exp. Med. 189, 741–746.
Nalabotu, S.K., Kolli, M.B., Triest, W.E., Ma, J.Y., Manne, N.D., Katta, A., Addagarla, H.S., Rice, K.M., Blough, E.R., 2011. Intratracheal instillation of cerium oxide nanoparticles induces hepatic toxicity in male Sprague–Dawley rats. Int. J. Nanomed. 6, 2327–2335.
Ohtomo, K., Wang, S., Masunaga, A., Aikichi, Iwamoto, Sugawara, I., 2000. Secondary infections of AIDS autopsy cases in Japan with special emphasis on Mycobacterium avium-intracellular complex infection. Tohoku J. Exp. Med. 192, 99–109.
Pal, S., Pal, P.B., Das, J., Sil, P.C., 2011. Involvement of both intrinsic and extrinsic pathways in hepatoprotection of arjunolic acid against cadmium induced acute damage in vitro. Toxicology 283, 129–139.
Park, B., Donaldson, K., Duffin, R., Tran, L., Kelly, F., Mudway, I., Morin, J.P., Guest, R., Jenkinson, P., Samaras, Z., Giannouli, M., Kouridis, H., Martin, P., 2008. Hazard and risk assessment of a nanoparticulate cerium oxide-based diesel fuel additive — a case study. Inhal. Toxicol. 20, 547–566.
Park, E.J., Yoon, J., Choi, K., Yi, J., Park, K., 2009. Induction of chronic inflammation in mice treated with titanium dioxide nanoparticles by intratracheal instillation. Toxicology 260, 37–46.
Park, E.J., Roh, J., Kim, S.N., Kang, M.S., Lee, B.S., Kim, Y., Choi, S., 2011. Biological toxicity and inflammatory response of semi-single-walled carbon nanotubes. PLoS One 6 (10), e25892.
Peng, S.F., Tseng, M.T., Ho, Y.C., Wei, M.C., Liao, Z.X., Sung, H.W., 2011. Mechanisms of cellular uptake and intracellular trafficking with chitosan/DNA/poly(gamma-glutamic acid) complexes as a gene delivery vector. Biomaterials 32, 239–248.
Pierscionek, B.K., Li, Y., Yasseen, A.A., Colhoun, L.M., Schachar, R.A., Chen, W., 2010. Nanoceria have no genotoxic effect on human lens epithelial cells. Nanotechnology 21, 035102.
Poon, H.F., Calabrese, V., Scapagnini, G., Butterfield, D.A., 2004. Free radicals: key to brain aging and heme oxygenase as a cellular response to oxidative stress. J. Gerontol. A Biol. Sci. Med. Sci. 59, 478–493.
Sadauskas, E., Danscher, G., Stoltenberg, M., Vogel, U., Larsen, A., Wallin, H., 2009. Protracted elimination of gold nanoparticles from mouse liver. Nanomedicine 5, 162–169.
Sadauskas, E., Wallin, H., Stoltenberg, M., Vogel, U., Doering, P., Larsen, A., Danscher, G., 2007. Kupffer cells are central in the removal of nanoparticles from the organism. Part. Fibre Toxicol. 4, 10.
Saunders, B.M., Cooper, A.M., 2000. Restraining mycobacteria: role of granulomas in mycobacterial infections. Immunol. Cell Biol. 78, 334–341.
Schreiber, H.A., Hulseberg, P.D., Lee, J., Prechl, J., Barta, P., Szlavik, N., Harding, J.S., Fabry, Z., Sandor, M., 2010. Dendritic cells in chronic mycobacterial granulomas restrict local anti-bacterial T cell response in a murine model. PLoS One 5, e11453.
Shaikh, Z.A., Vu, T.T., Zaman, K., 1999. Oxidative stress as a mechanism of chronic cadmium-induced hepatotoxicity and renal toxicity and protection by antioxidants. Toxicol. Appl. Pharmacol. 154, 256–263.
Si-Tayeb, K., Lemaigre, F.P., Duncan, S.A., 2010. Organogenesis and development of the liver. Dev. Cell 18, 175–189.
Siciliano, A., Malpeli, G., Platt, O.S., Lebouef, C., Janin, A., Scarpa, A., Olivieri, O., Amato, E., Corrocher, R., Beuzard, Y., De Franceschi, L., 2011. Abnormal modulation of cell protective systems in response to ischemic/reperfusion injury is important in the development of mouse sickle cell hepatopathy. Haematol-Hematol. J. 96, 24–32.
Sinha-Hikim, I., Shen, R., Nzenwa, I., Gelfand, R., Mahata, S.K., Sinha-Hikim, A.P., 2011. Minocycline suppresses oxidative stress and attenuates fetal cardiac myocyte apoptosis triggered by in utero cocaine exposure. Apoptosis 16, 563–573.
Taniguchi, M., Yasutake, A., Takedomi, K., Inoue, K., 1999. Effects of N-nitrosodimethylamine (NDMA) on the oxidative status of rat liver. Arch. Toxicol. 73, 141–146.
Toussaint, O., Houbion, A., Remacle, J., 1993. Relationship between the critical-level of oxidative stresses and the glutathione-p activity. Toxicology 81, 89–101.
Ushitora, M., Sakurai, F., Yamaguchi, T., Nakamura, S., Kondoh, M., Yagi, K., Kawabata, K., Mizuguchi, H., 2010. Prevention of hepatic ischemia-reperfusion injury by pre-administration of catalase-expressing adenovirus vectors. J. Control. Release 142, 431–437.
Wang, J., Chen, C., Lau, S., Raghavan, R.I., Rowsell, E.H., Said, J., Weiss, L.M., Huang, Q., 2009. CD3-positive large B-cell lymphoma. Am. J. Surg. Pathol. 33, 505–512.
Warren, A., Benseler, V., Cogger, V.C., Bertolino, P., LE Couteur, D.G., 2011. The impact of poloxamer 407 on the ultrastructure of the liver and evidence for clearance by extensive endothelial and Kupffer Cell endocytosis. Toxicol. Pathol. 39, 390–397.
Wick, P., Manser, P., Limbach, L.K., Dettlaff-Weglikowska, U., Krumeich, F., Roth, S., Stark, W.J., Bruinink, A., 2007. The degree and kind of agglomeration affect carbon nanotube cytotoxicity. Toxicol. Lett. 168, 121–131.
Winterstein, J., Basu, J., Herzing, A., Anderson, I., Carter, C., 2008. Combined structural and chemical investigations of ceria nanoparticles in the TEM. Microsc. Microanal. 14, 280–281.
Yokel, R.A., Florence, R.L., Unrine, J.M., Tseng, M.T., Graham, U.M., Wu, P., Grulke, E.A., Sultana, R., Hardas, S.S., Butterfield, D.A., 2009. Biodistribution and oxidative stress effects of a systemically-introduced commercial ceria engineered nanomaterial. Nanotoxicology 3, 234–248.
Yokel, R.A., Au, T.C., MacPhail, R., Hardas, S.S., Butterfield, D.A., Sultana, R., Tseng, M.T., Dan, M., Florence, R.L., Unrine, J.M., Graham, U.M., Wu, P., Grulke, E.A., 2012. Distribution, elimination and biopersistence to 90 days of a systemically-introduced 30 nm ceria engineered nanomaterial in rats. Toxicol Sci. doi:10.1093/toxsci/kfs067.
Yokota, S., Takashima, H., Ohta, R., Saito, Y., Miyahara, T., Yoshida, Y., Negura, T., Senuma, M., Usumi, K., Hirabayashi, N., Watanabe, T., Horiuchi, S., Fujitani, Y., Hirano, S., Fujimaki, H., 2011. Nasal instillation of nanoparticle-rich diesel exhaust particles slightly affects emotional behavior and learning capability in rats. J. Toxicol. Sci. 36, 267–276.
Yun, N., Eum, H.A., Lee, S.M., 2010. Protective role of heme oxygenase-1 against liver damage caused by hepatic ischemia and reperfusion in rats. Antioxid. Redox Signal. 13, 1503–1512.
Zhan, Y., Wang, Y., Wei, L., Chen, H., Cong, X., Fei, R., Gao, Y., Liu, F., 2006. Differentiation of hematopoietic stem cells into hepatocytes in liver fibrosis in rats. Transplant. Proc. 38, 3082–3085.
Zhang, J.S., Liu, F., Huang, L., 2005. Implications of pharmacokinetic behavior of lipoplex for its inflammatory toxicity. Adv. Drug Deliv. Rev. 57, 689–698.